nature materials

SUPPLEMENTARY INFORMATION

https://doi.org/10.1038/s41563-019-0424-2

In the format provided by the authors and unedited.

Electric field control of Néel spin–orbit torque in an antiferromagnet

Xianzhe Chen[1,5], Xiaofeng Zhou[1,5], Ran Cheng[2,5], Cheng Song[1*], Jia Zhang[3], Yichuan Wu[3], You Ba[4], Haobo Li[4], Yiming Sun[1], Yunfeng You[1], Yonggang Zhao[4] and Feng Pan[1*]

[1]Key Laboratory of Advanced Materials (MOE), School of Materials Science and Engineering, Tsinghua University, Beijing, China. [2]Department of Electrical and Computer Engineering, University of California, Riverside, CA, USA. [3]School of Physics and Wuhan National High Magnetic Field Center, Huazhong University of Science and Technology, Wuhan, China. [4]State Key Laboratory of Low-Dimensional Quantum Physics and Department of Physics, Tsinghua University, Beijing, China. [5]These authors contributed equally: X. Chen, X. Zhou, R. Cheng. *e-mail: songcheng@mail.tsinghua.edu.cn; panf@mail.tsinghua.edu.cn

Supplementary Materials for

Electric field control of Néel spin-orbit torque in an antiferromagnet

Xianzhe Chen[1,†], Xiaofeng Zhou[1,†], Ran Cheng[2,†], Cheng Song[1,*], Jia Zhang[3], Yichuan Wu[3], You Ba[4], Haobo Li[4], Yiming Sun[1], Yunfeng You[1], Yonggang Zhao[4], Feng Pan[1,*]

[1] Key Laboratory of Advanced Materials (MOE), School of Materials Science and Engineering, Tsinghua University, Beijing 100084, China

[2] Department of Physics and Astronomy, University of California, Riverside, California 92521, USA

[3] School of Physics and Wuhan National High Magnetic Field Center, Huazhong University of Science and Technology, Wuhan 430074, China

[4] State Key Laboratory of Low-Dimensional Quantum Physics and Department of Physics, Tsinghua University, Beijing 100084, China

Simulations

We take the Heisenberg exchange coupling between A and B sublattices (in angular frequency) to be $\omega_J = 2\pi \times 15$ THz[S1] and the Gilbert damping to be $\alpha = 0.0025$ [S2]. It can be read off from our first-principle calculations as shown below that $K_{2\perp} = -2.3$ meV and $K_{4\parallel} = 3\ \mu$eV. The $K_{2\parallel}$ term can be read off either from Fig. S5 or by comparing the changes of threshold current density shown in Fig. 4a and 4b. In the former, by comparing the MAE at $\varphi = 0$ and $\varphi = \pi/2$, we are able to tell that $K_{2\parallel} \approx 7\mu$eV. In the latter method, we observe that the threshold current densities essentially reverse their positions in the two subfigures, indicating that $K_{2\parallel}$ is around half of the change in ΔK_g when sweeping the electric field from 4 kV/cm to –2 kV/cm. The field-induced anisotropy $\Delta K_g = 0$ at E = 4 kV/cm and $\Delta K_g \approx 0.014$

meV at E = –2 kV/cm, thus $K_{2\parallel} \approx 7\,\mu$eV, which is consistent with the previous method. The specific form of ΔK_g as a function of the electric field cannot be determined exactly, so we extract it directly from the measurement by strain gauge. Finally, the amplitude of the field-like NSOT ($\omega_{sA} = -\omega_{sB}$) as a function of the applied current density can be obtained from available studies[S3,S4]. The simulation follows a similar algorithm and procedure of previous report[S5].

In-plane strains characterized with strain gauge

A strain gauge was used to measure the in-plane remanent strain of the PMN-PT(011) substrate driven by the electric field. Corresponding data are displayed in Fig. S1, where *x* and *y* axes are along the [0$\bar{1}$1] and [100] directions of the PMN-PT(011) substrate, respectively. For this experiment, the nonvolatile strain of PMN-PT along *x* and *y* axes were obtained as a function of electric field from +4 to –4 kV/cm and then from –4 to +4 kV/cm. Noted that each electric field was applied with voltage pulse, the remanent strain was measured after removing the applied electric fields. When the electric field is swept from +4 to –2 kV/cm, the PMN-PT substrate and the adjacent Mn_2Au films are elongated along *x* axis and compressive along *y* axis accordingly. The electric field-dependent remanent strain ε shows a symmetric butterfly-like shape. The maximum strain ε_x along the *x* axis is around 0.06 % (Fig. S1A) and its counterpart ε_y along the *y* axis is approximately –0.02 % (Fig. S1B) at the electric field of around ±2 kV/cm. The in-plane strain ε_{x-y} (Fig. S1C) is then obtained, which is defined to be the difference between ε_x and ε_y at the same electric field, e.g., ε_{x-y} = 0.08%, irrespective of +2 or –2 kV/cm. Although the variation tendency of the strain can be revealed by the strain gauge, the real strain of the sample is commonly underestimated by the strain gauge[S6].

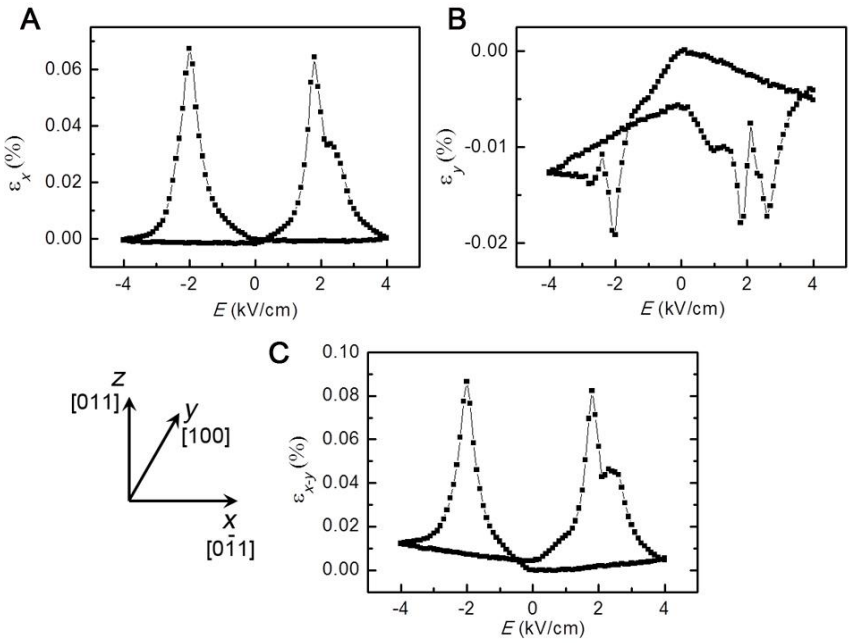

Fig. S1 In-plane remanent strain measured by strain gauge. The strain ε_x (along [0$\bar{1}$1] axis) (**A)** ε_y (along [100] axis) **(B)** and their difference ε_{x-y} **(C)** are shown as a function of pulsed electric field *E*, which is swept from +4 to –4 kV/cm and then from –4 to 4 kV/cm.

We also measure the "volatile" strain of the sample when the electric field is applied. Figure S2A and S2B display the "volatile" strain along the [0$\bar{1}$1] (*x*-axis) and [100] (*y*-axis), respectively, as a function of electric field *E*, which is swept from +4 to –4 kV/cm and then from –4 to 4 kV/cm. As compared with the nonvolatile counterpart in Fig. S1A, the strain ε_x along the *x*-axis is similar, with the maximum value around 0.06%. Nevertheless the "volatile" strain ε_y shown in Fig. S2B is different from the nonvolatile one in Fig. S1B. The compressive strain value increases from 0.02% to 0.07%, reflecting an additional compressive strain along [100], compared to the nonvolatile counterpart. This results in a distinctive in-plane strain with the electric field on (Fig. S2C). Note that it is more challenging to measure Néel order reliably when the electric field is applied, because the existence of the electric

field might complicate the XMLD measurements in total electron yield mode and Néel moments switching-induced Hall signals.

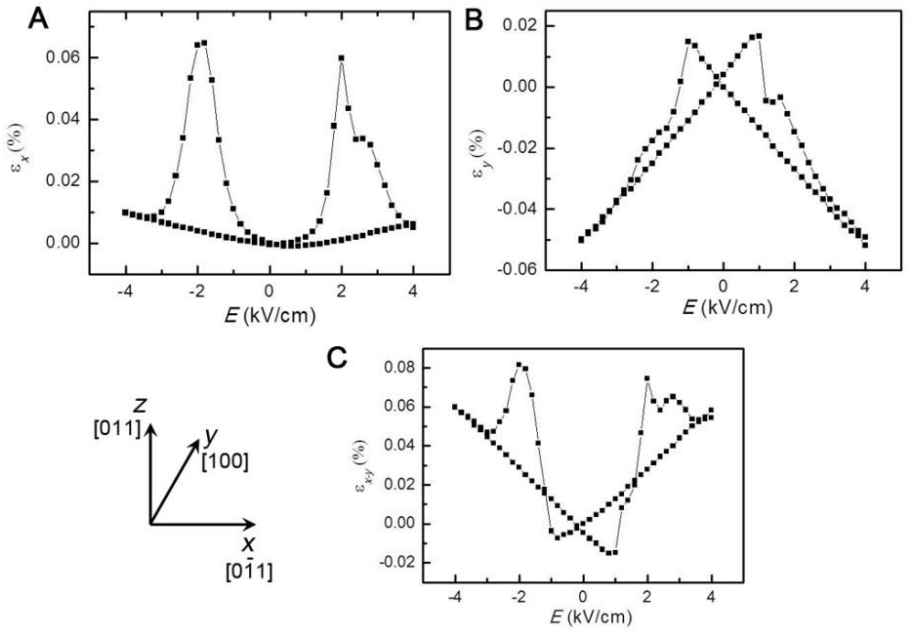

Fig. S2 In-plane volatile strain measured with electric fields on. The strain ε_x (along [0$\bar{1}$1] axis) (**A)** ε_y (along [100] axis) **(B)** and their difference ε_{x-y} **(C)** are shown as a function of electric field *E*, which is swept from +4 to –4 kV/cm and then from –4 to 4 kV/cm.

Reciprocal space maps of PMN-PT(011) after different electric fields

The reciprocal space mapping (RSM) of the Mn_2Au/PMN-PT (011) samples were characterized by x-ray diffractometer (XRD, Rigaku, Smartlab). RSM is a powerful method to quantify the strain state, which has widely applied when demonstrating the strain state of the ferroelectric materials[S7]. Figure S3A displays a schematic of applying electric field on the Mn_2Au/PMN-PT samples in the (400) crystalline plane where half of the PMN-PT thin film (2.5 × 5 mm^2) is covered with the bottom electrode. With this setup, the half of the sample maintains at the pristine state as reference, meanwhile the x-ray spot size in the RSM measurements is 10 × 5 mm^2,

which guarantees the simultaneous measurements of lattice parameters for the original state and the electric field acting area.

Apparently, when applying the electric field of +4 kV/cm and then switching it off, there are two separated diffraction peaks in Fig. S3B. The lattice parameters of PMN-PT along [0$\bar{1}$1] and [011] axis could be calculated from RSM patterns. The top left peak ($Q_{[0\bar{1}1]}$=0.7041, $Q_{[011]}$=0.7045) and the low right peak ($Q_{[0\bar{1}1]}$=0.7054, $Q_{[011]}$=0.7027) correspond to the original state and the +4 kV/cm state of PMN-PT (011), respectively. The in-plane lattice variation along the [0$\bar{1}$1] axis is calculated to be ~0.2%, coinciding with the previous report[S7]. Differently, after applying the electric field of –2 kV/cm, only one peak ($Q_{[0\bar{1}1]}$=0.7036, $Q_{[011]}$=0.7041) is visible in Fig. S3C, suggesting that the strain state after –2 kV/cm is analogous to that of the original state.

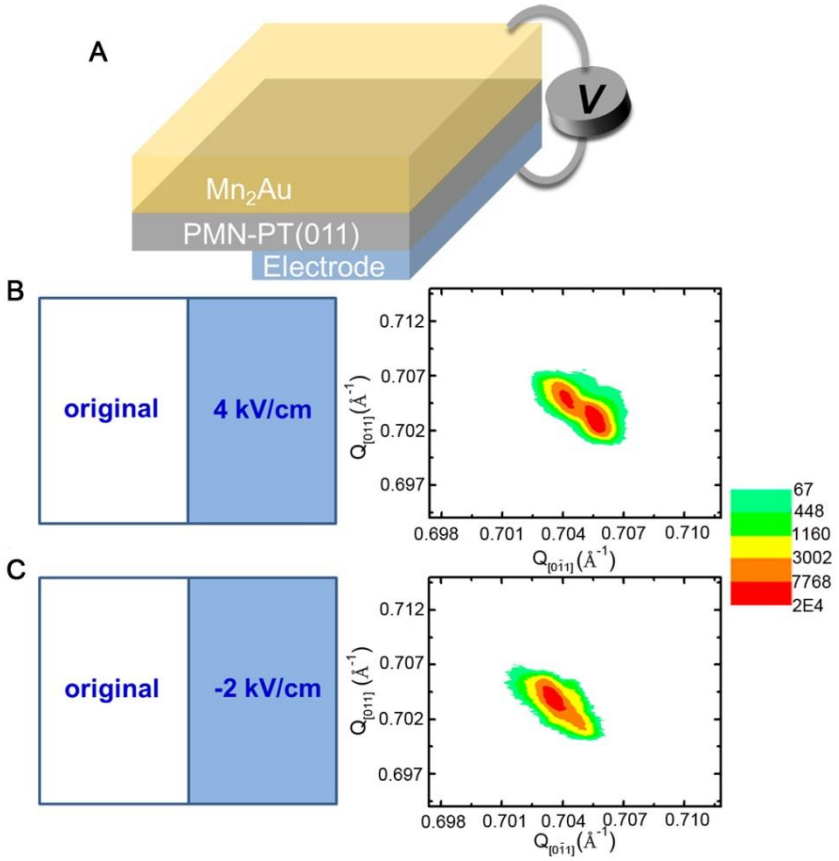

Fig. S3 X-ray reciprocal space map (RSM) of PMN-PT (400) plane. (**A**) Schematic of

applying electric field on Mn_2Au(103)/PMN-PT(011) samples. The bottom electrode covers one half the PMN-PT substrate. (**B**), (**C**) RSM results are obtained via applying electric fields of +4 kV/cm (**B**) and –2 kV/cm (**C**) on the Mn_2Au/PMN-PT samples and then switching it off.

First-principle calculations of the magnetocrystalline anisotropic energy of strained Mn_2Au

The first-principles calculations were carried out by using the plane wave based Vienna ab initio simulation package (VASP)[S8]. The Perdew-Burke-Ernzerhof (PBE) generalized gradient approximation (GGA)[S9] was used for the exchange-correlation potential and projected augmentation wave (PAW)[S10] scheme for constructing pseudo potential. The atomic positions of Mn_2Au at different lattice constant are fully relaxed until the force on each atom is less than 0.1 meV/Å.

For the magnetocrystalline anisotropic energy (MAE) calculations, a standard force theory is adopted which is proved to be a successful method to deal with the MAE in magnetic metallic system[S11,S12]. First, a self-consistence calculation of electron charge density is achieved in the absence of spin-orbit coupling. And then it is followed by a one-step calculation including spin-orbit coupling with the magnetization aligning along desired directions. The MAE is eventually evaluated by taking the band energy difference. The convergence of MAE respecting to the number of k-point has been checked, and a k-point mesh of $30 \times 30 \times 11$ with around 10000 k-points in Brillion zone is found to be necessary for MAE energy convergence within 1 μeV/f.c. (formula cell). The energy convergence criteria are better than 10^{-7} eV (0.1 μeV)[S11,S12].

Mn_2Au is an antiferromagnet with tetragonal structure. A unit cell of Mn_2Au is

illustrated in Fig. S4A. First-principle calculations of MAE per formula cell of strained Mn_2Au are conducted for the following 4 cases with different lattice parameters. When the lattice parameter of *a*-axis ([100]) is larger than that of *b*-axis ([010]), the strain is defined as positive, while the negative corresponds to the opposite scenario.

1. case 1, 0.15% strain: a = 0.3329 nm, b = 0.3324 nm, c = 0.8539 nm;
2. case 2, –0.12% strain: a = 0.3327 nm, b = 0.3331 nm, c = 0.8539 nm;
3. case 3, 0.27% strain: a = 0.3330 nm, b = 0.3321 nm, c = 0.8539 nm;
4. case 4, –0.27% strain: a = 0.3326 nm, b = 0.3335 nm, c = 0.8539 nm.

As presented in Fig. S4B, the MAE difference between *x*- and *y*-axes (ΔMAE_{x-y}) varies linearly with the in-plane strain ε_{x-y}, where ε_{x-y} ranges from –0.3% to 0.3%. The MAE of Mn_2Au along four typical magnetization axes is summarized in Table S1, where four strain states are included.

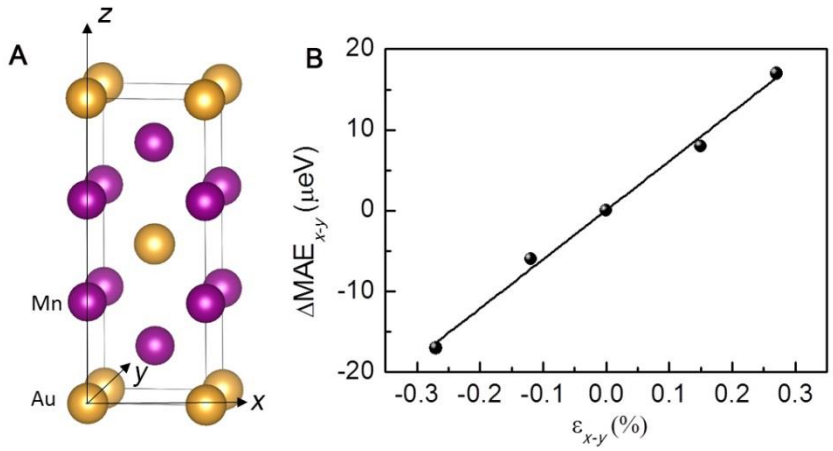

Fig. S4 MAE of Mn_2Au. (**A**) Tetragonal Mn_2Au cell. (**B**) MAE difference between *x*- and *y*-axes (ΔMAE_{x-y}) as a function of in-plane strain ε_{x-y}.

Table S1 MAE (in unit of meV) of strained Mn_2Au calculated for different magnetization axes. Easy axis is marked in red.

Magnetization axis	case 1	case 2	case 3	case 4
[001]	0	0	0	0
[100]	–2.315	**–2.312**	–2.333	**–2.310**
[110]	–2.313	–2.303	–2.345	–2.300
[010]	**–2.323**	–2.306	**–2.350**	–2.293

The angle-dependent MAE for four cases is shown in Fig. S5. In the Mn_2Au cells with strain, a common feature in Fig. S5B–S5E is that the lowest MAE emerges when the antiferromagnetic moments are aligned along the compressive in-plane axis, e.g., [010] axis for case 1 and [100] axis for case 2. Also visible is that the energy barrier remains when the strain is comparatively small (case 1 and case 2). However, with increasing strain (case 3 and case 4), MAE exhibits a monotonous variation when the antiferromagnetic moments rotate 90 °, from [100] to [010] axes.

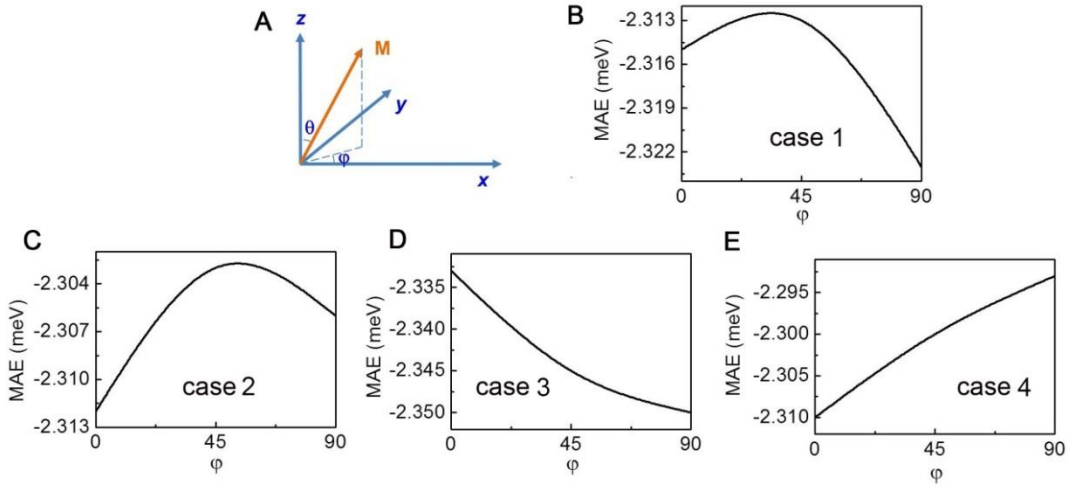

Fig. S5 Angle-dependent MAE of Mn_2Au. The axis rotates from [100] to [010] directions when compressive strain is applied along [010] axis of Mn_2Au.

X-ray diffraction spectra of Mn_2Au/PMN-PT(011)

Figure S6 shows the x-ray diffraction spectrum of 20 nm-thick Mn_2Au films grown on PMN-PT(011) substrate. Besides of the diffraction peaks from PMN-PT(011) substrate, only Mn_2Au (103) peak is visible, indicating the growth of (103)-oriented Mn_2Au films.

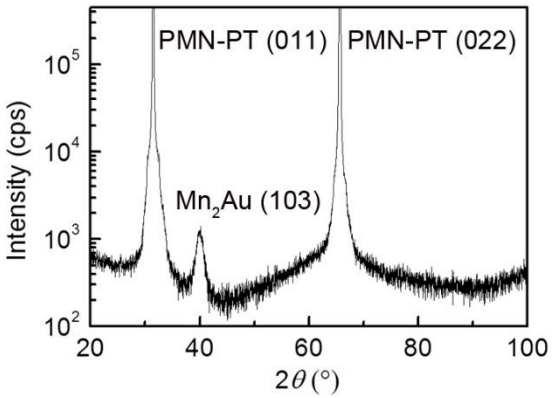

Fig. S6 X-ray diffraction spectrum of Mn_2Au/PMN-PT(011) samples.

Electric field-dependent Mn *L*-edge x-ray magnetic linear dichroism and planar Hall resistance

We show in Fig. S7 the XAS spectra with [100] (//) and [01$\bar{1}$] ($\perp$) polarization. The X-ray is vertically incident to the Mn_2Au film (Fig. S7A). The XMLD signals are obtained as $\mathrm{XMLD} = \mathrm{XAS}_{//} - \mathrm{XAS}_{\perp}$, where $\mathrm{XAS}_{//}$ and $\mathrm{XAS}_{\perp}$ denote the x-ray absorption spectroscopy (XAS) recorded with [100] (//) and [0$\bar{1}$1] ($\perp$) polarization, respectively, as illustrated in Fig. 2A. Note that the spectra were recorded *in-situ* at zero-field after applying the electric field marked above each spectrum in Fig. S7. $\mathrm{XAS}_{//}$ and $\mathrm{XAS}_{\perp}$ and corresponding XMLD (×5) are shown for the original states (Fig. S7B), the state after +4 kV/cm (Fig. S7C), the state after –2 kV/cm (Fig. S7D). More details can be found in the main text.

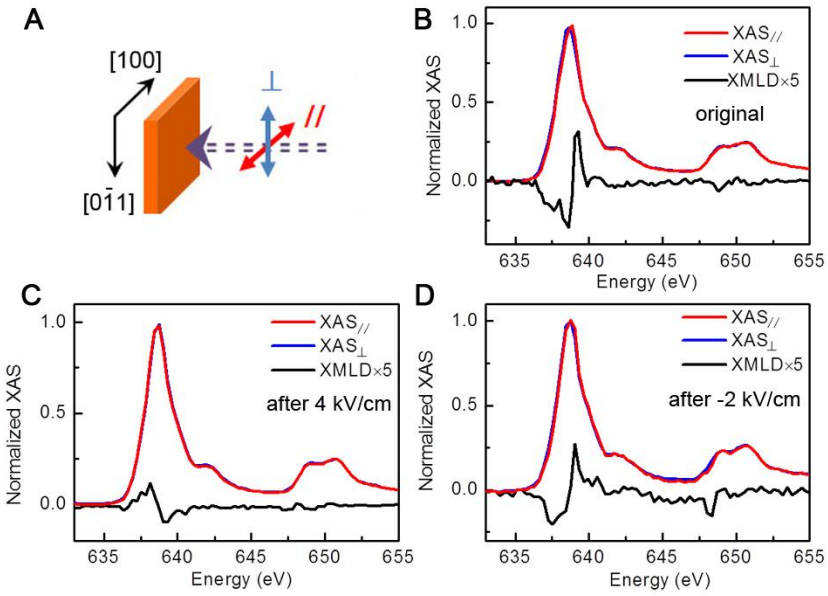

Fig. S7 XAS and corresponding XMLD spectra recorded after applying different electric fields. (**A**) The x-ray is vertically incident to the Mn_2Au film. XAS recorded with [100] (//) and [01$\bar{1}$] (⊥) polarization are shown in (**B**) original state, (**C**) after +4 kV/cm, (**D**) after –2 kV/cm. Concomitant XMLD curves are shown below in each panel.

The planar Hall effect is used to electrically detect the Néel order switching. The measurement configurations are illustrated in the inset of Fig. S8A and the offset of the Hall resistance in Fig. S8A was subtracted from the raw data. Remarkably, after applying electric field of –2 kV/cm with the pulse width of 500 ms, the Hall resistance variation (ΔR_{xy}) drops from a high (positive) to low (negative) resistive state, which is due to the Néel order switching from [0$\bar{1}$1] to [100], according to the analysis of the planar Hall effect. Note that the variation is sharp with negligible thermal relaxation. Also visible is that the retention time of ΔR_{xy} is up to one hour without any obvious degradation. ΔR_{xy} undergoes a sudden jump after gated with E = +4 kV/cm, which recovers the previous +4 kV/cm counterpart, indicating the switching of the Néel

order back to [0$\bar{1}$1]. We show in Fig. S8B the reversible ΔR_{xy} variation as a function of the alternative action of E = +4 kV/cm and –2 kV/cm, indicating the switching of the Néel order between two orthogonal axes in ten circles.

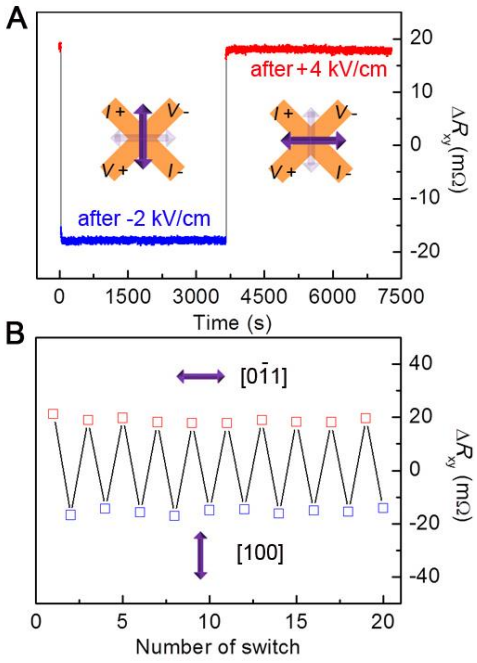

Fig. S8 (**A**) Nonvolatile Hall resistance variations induced by voltage pulses (after –2 kV/cm and +4 kV/cm). Each state was recorded for one hour. (**B**) Reversible change of two Hall resistance states (after –2 kV/cm and +4 kV/cm) in ten circles.

The smoothed x-ray magnetic linear dichroism (XMLD) spectra are recorded after applying different electric fields, which is swept from +4 to –4 kV/cm (Fig. S9A), and then back to +4 kV/cm (Fig. S9B). For this experiment, the x-ray was vertically incident to the film and the polarized direction of the x-ray is parallel to the (011) plane of the PMN-PT substrate. With decreasing E from +4 to –0.6 kV/cm, the values of ΔXMLD keep positive, where $\Delta\text{XMLD} = \text{XMLD}_{@638} - \text{XMLD}_{@639}$, defined by the difference between two extreme values (peak or valley) at ~638 and ~639 eV at L_3-edge. Further decreasing E to –1.6 kV/cm, the ΔXMLD value turns out to be negative, followed by the negative maximum at E = –2.4 kV/cm, and then goes back

to be positive at E = –4 kV/cm. With increasing E, a transition of the ΔXMLD value from positive to negative as E is just above zero, accompanied by the negative maximum at E = +3.4 kV/cm, and then the ΔXMLD value approaches the originally positive value at E = +4 kV/cm. A summary of the electric field dependent ΔXMLD is shown in Fig. 2C in the main text, which exhibits a butterfly shape.

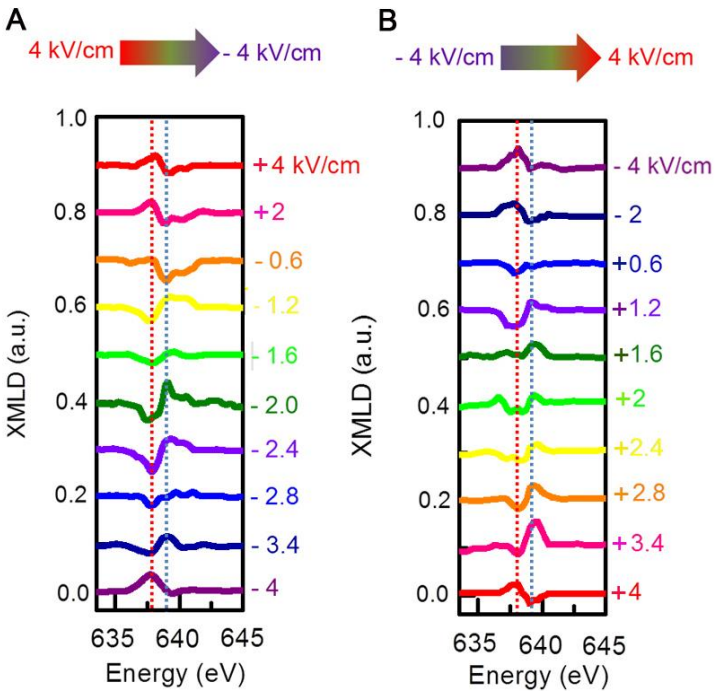

Fig. S9 XMLD spectra recorded after applying different electric fields. Electric fields were swept from +4 to –4 kV/cm (**A**) and then from –4 to +4 kV/cm (**B**).

Electric field-dependent Mn *L*-edge x-ray magnetic linear dichroism of IrMn/PMN-PT(011) sample

As a control experiment, we performed XMLD measurements on 20 nm-thick IrMn films grown on PMN-PT(011) substrate, where identical experimental conditions were used as Mn_2Au case. Note that the XMLD signal of IrMn varies somehow at different ferroelastic strain state, after +4 kV/cm (Fig. S10A) and –2 kV/cm (Fig. S10B), but there is no polarity reversal, because of its comparatively

strong in-plane magnetic anisotropy and the correspondingly negligible Néel moments switching.

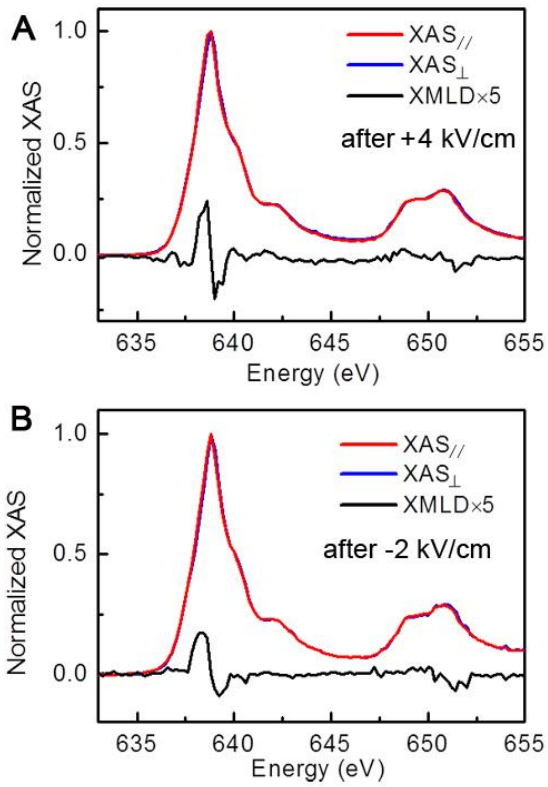

Fig. S10 XAS and concomitant XMLD spectra recorded after applying different electric fields on IrMn/PMN-PT(011). (**A**) after +4 kV/cm, (**B**) after –2 kV/cm.

S1. A. B. Shick *et al.*, *Phys. Rev. B* **81**, 212409 (2010).

S2. N. Bhattacharjee *et al.*, *Phys. Rev. Lett.* **120**, 237201 (2018).

S3. P. Wadley *et al.*, *Science* **351**, 587 (2016).

S4. J. Železný *et al.*, *Phys. Rev. Lett*. **113**, 157201 (2014).

S5. R. Cheng, M. W. Daniels, J.-G. Zhu, and D. Xiao, *Phys. Rev. B* **91**, 064423 (2015).

S6. A. T. Chen *et al.*, *Adv. Mater*. **28**, 363 (2016).

S7. M. Liu *et al.*, *Adv. Mater.* **25**, 4886 (2013).

S8. G. Kresse *et al.*, *Phys. Rev. B* **54**, 11169 (1996).

S9. J. P. Perdew, K. Burke and M. Ernzerhof, *Phys. Rev. Lett.* **77**, 3865 (1996).

S10. D. Hobbs, G. Kresse and J. Hafner, *Phys. Rev. B* **62**, 11556 (2000).

S11. J. Zhang, C. Franz, M. Czerner and C. Heiliger, *Phys. Rev. B* **90**, 184409 (2014).

S12. J. Zhang, P. V. Lukashev, S. S. Jaswal and E. Y. Tsymbal. *Phys. Rev. B* **96**, 014435 (2017).